

Micron-resolved quantum precision measurement of magnetic field at the Tesla level

Si-Han An(安思瀚), Shi-Yu Ge(葛仕宇), Wen-Tao Lu(卢文韬), Guo-Bin Chen(陈国彬), Sheng-Kai Xia(夏圣开), Ai-Qing Chen(陈爱庆), Cheng-Kun Wang(王成坤), Lin-Yan Yu(虞林嫣), Zhi-Qiang Zhang(张致强), Yang Wang(汪洋), Gui-Jin Tang(唐贵进), Hua-Fu Cheng(程华富), and Guan-Xiang Du(杜关祥)

Citation: Chin. Phys. B, 2024, 33 (**12**): 120305. DOI: 10.1088/1674-1056/ad7e9b
Journal homepage: http://cpb.iphy.ac.cn; http://iopscience.iop.org/cpb

What follows is a list of articles you may be interested in

Orientation determination of nitrogen-vacancy center in diamond using a static magnetic field

Yangpeng Wang(王杨鹏), Rujian Zhang(章如健), Yan Yang(杨燕), Qin Wu(吴琴), Zhifei Yu(于志飞), and Bing Chen(陈冰)
Chin. Phys. B, 2023, 32 (**7**): 070301. DOI: 10.1088/1674-1056/acc0f7

Heralded entanglement purification protocol using high-fidelity parity-check gate based on nitrogen-vacancy center in optical cavity

Lu-Cong Lu(陆路聪), Guan-Yu Wang(王冠玉), Bao-Cang Ren(任宝藏), Mei Zhang(章梅), Fu-Guo Deng(邓富国)
Chin. Phys. B, 2020, 29 (**1**): 010305. DOI: 10.1088/1674-1056/ab5939

Experimental implementation of a continuous-time quantum random walk on a solid-state quantum information processor

Maimaitiyiming Tusun(麦麦提依明·吐孙), Yang Wu(伍旸), Wenquan Liu(刘文权), Xing Rong(荣星), Jiangfeng Du(杜江峰)
Chin. Phys. B, 2019, 28 (**11**): 110302. DOI: 10.1088/1674-1056/ab44ae

Quantum information processing with nitrogen-vacancy centers in diamond

Gang-Qin Liu(刘刚钦), Xin-Yu Pan(潘新宇)
Chin. Phys. B, 2018, 27 (**2**): 020304. DOI: 10.1088/1674-1056/27/2/020304

A high-fidelity memory scheme for quantum data buses

Bo-Yang Liu(刘博阳), Wei Cui(崔巍), Hong-Yi Dai(戴宏毅), Xi Chen(陈希), Ming Zhang(张明)
Chin. Phys. B, 2017, 26 (**9**): 090303. DOI: 10.1088/1674-1056/26/9/090303

INSTRUMENTATION AND MEASUREMENT

Micron-resolved quantum precision measurement of magnetic field at the Tesla level

Si-Han An(安思瀚)[1], Shi-Yu Ge(葛仕宇)[1], Wen-Tao Lu(卢文韬)[2], Guo-Bin Chen(陈国彬)[3], Sheng-Kai Xia(夏圣开)[4], Ai-Qing Chen(陈爱庆)[1], Cheng-Kun Wang(王成坤)[1], Lin-Yan Yu(虞林嫣)[1], Zhi-Qiang Zhang(张致强)[1], Yang Wang(汪洋)[5], Gui-Jin Tang(唐贵进)[1], Hua-Fu Cheng(程华富)[6], and Guan-Xiang Du(杜关祥)[1,†]

[1] *College of Telecommunications and Information Engineering, Nanjing University of Posts and Telecommunications, Nanjing* 210003, *China*
[2] *Portland Institute, Nanjing University of Posts and Telecommunications, Nanjing* 210023, *China*
[3] *The School of Mechanical and Electrical Engineering, Suqian College, Suqian* 223800, *China*
[4] *School of Computer Science, Nanjing University of Posts and Telecommunications, Nanjing* 210023, *China*
[5] *School of Science, Nanjing University of Posts and Telecommunications, Nanjing* 210023, *China*
[6] *Yichang Testing Technique R&D Institute, Yichang* 443003, *China*

(Received 29 July 2024; revised manuscript received 20 September 2024; accepted manuscript online 24 September 2024)

We develop a quantum precision measurement method for magnetic field at the Tesla level by utilizing a fiber diamond magnetometer. Central to our system is a micron-sized fiber diamond probe positioned on the surface of a coplanar waveguide made of nonmagnetic materials. Calibrated with a nuclear magnetic resonance magnetometer, this probe demonstrates a broad magnetic field range from 10 mT to 1.5 T with a nonlinear error better than 0.0028% under a standard magnetic field generator and stability better than 0.0012% at a 1.5 T magnetic field. Finally, we demonstrate quantitative mapping of the vector magnetic field on the surface of a permanent magnet using the diamond magnetometer.

Keywords: nitrogen-vacancy center, fiber diamond magnetometer, precision measurement

PACS: 03.67.–a, 03.65.Yz, 75.50.Ww **DOI:** 10.1088/1674-1056/ad7e9b

1. Introduction

The precise measurement of strong magnetic fields has extensive applications in various domains, including cosmic engineering, industrial manufacturing, materials science and medicine.[1–5] Currently, the Hall effect[6] and nuclear magnetic resonance (NMR)[7] are the predominant techniques employed for this purpose. However, NMR is not capable of measuring vector magnetic fields, and its millimeter-level spatial resolution (~ 4 mm) restricts the gradient range of the measured magnetic field ($\sim 10^{-3}$ cm^{-1}), resulting in low sensitivity to non-uniform magnetic fields. Hall sensors suffer from temperature drift and aging and need periodic calibration, not being self-calibrated. Thus there is an urgent need to develop novel magnetic measurement techniques with high spatial resolution and quantum calibration.

As a magnetic quantum sensor with a broad spectrum (DC–GHz), remarkable sensitivity, and unprecedented spatial resolution (theoretical limit ~ 1 nm), a diamond nitrogen-vacancy (NV) center magnetometer can perform nanomagnetic imaging on a few nuclear spins, including two-dimensional magnetic materials, current distribution, conductivity distribution and even individual electron spins.[8] At present, research on magnetic imaging based on NV centers has mainly focused on weak DC magnetic fields[9,10] and microwave magnetic fields.[11,12] In this work, we propose a novel NV center magnetometer covering the measurement range of 10 mT to 1.5 T, particularly for quantum precision measurement of strong magnetic fields.

Our research introduces an integrated probe with a micron-sized diamond crystal coupled to a tapered fiber tip,[13,14] which is carefully positioned on the surface of a nonmagnetic microwave coplanar waveguide under a microscope. The waveguide, operating up to 45 GHz and beyond, is fabricated with a standard printed circuit board process. The tapered fiber is crucial for efficient collection of fluorescence photons emitted by the micronsized diamond crystal. The whole assembly has a typical volume of around 2 cm^3 and is light in weight, offering practical convenience in magnetic field metrology and characterization of magnetic materials.

2. Basic theory and experimental setup

An NV center is formed in a diamond lattice by the substitution of two adjacent carbon sites by a nitrogen atom and a vacancy and the capture of an additional electron, forming a negatively charged defect center. The energy levels are seated within the crystal band gap. The NV center possesses an elec-

†Corresponding author. E-mail: duguanxiang@njupt.edu.cn

© 2024 Chinese Physical Society and IOP Publishing Ltd

tron spin triplet state, detectable through optically detected magnetic resonance (ODMR).[15] The Hamiltonian of the NV center is affected by the simultaneous presence of an external magnetic field and temperature,[16,17] and it is expressed as follows:

$$H = DS_z^2 + \boldsymbol{B}\cdot\boldsymbol{S} + E\left(S_x^2 - S_y^2\right), \tag{1}$$

where $\boldsymbol{B} = \gamma_e \boldsymbol{B}'$, $\boldsymbol{B}'$ is the magnetic field strength, $\gamma_e = -2.802495$ MHz·G^{-1} is the electron gyromagnetic ratio, D is the axial zero-field splitting and $\boldsymbol{S} = (S_x, S_y, S_z)$ is the Pauli spin matrix. For a NV axis, we define the angle between the magnetic field and the NV axis as θ, and $\boldsymbol{B}' = B(\sin\theta\hat{\boldsymbol{x}} + \cos\theta\hat{\boldsymbol{z}})$. Combine Eq. (1) and the following equation:

$$H' = H - \frac{2}{3}I, \tag{2}$$

where I is the identity matrix and H' is a matrix with the same rank as the Hamiltonian matrix H after transformation, for the purpose of simplifying calculations. The expression for H' is given by

$$H' = \begin{pmatrix} \frac{D}{3} + B\cos\theta & \frac{1}{\sqrt{2}}B\sin\theta & E \\ \frac{1}{\sqrt{2}}B\sin\theta & -\frac{2D}{3} & \frac{1}{\sqrt{2}}B\sin\theta \\ E & \frac{1}{\sqrt{2}}B\sin\theta & \frac{D}{3} - B\cos\theta \end{pmatrix}. \tag{3}$$

The eigenfrequencies $f_{i=1,2,3}$ of H' can be found from its characteristic polynomial

$$f^3 - \left(\frac{D^2}{3} + B^2 + E^2\right) f + \frac{1}{2}B^2\cos 2\theta\,(E-D) - \frac{1}{2}EB^2 - \frac{1}{6}DB^2 - \frac{2}{3}DE^2 + \frac{2}{27}D^3 = 0, \tag{4}$$

which should be factorized according to

$$\begin{aligned} &(f-f_1)(f-f_2)(f-f_3) \\ &= f^3 - (f_1+f_2+f_3)f^2 + (f_1f_2 + f_1f_3 + f_2f_3)f - f_1f_2f_3 \\ &= 0. \end{aligned} \tag{5}$$

In a strong magnetic field environment ($B > 1000$ G), we have

$$f_U = f_3 - f_1, \quad f_L = f_2 - f_1, \tag{6}$$

where f_U and f_L are the peak frequencies of the upper and lower peaks, respectively, in the ODMR spectrum corresponding to an NV axis. Comparing the linear terms of Eq. (4), we can obtain

$$B = \frac{1}{\sqrt{3}}\sqrt{f_U^2 + f_L^2 - f_U f_L - D^2 - 3E^2}. \tag{7}$$

Comparing the constant term of Eq. (5), we can obtain

$$\cos^2\theta = \frac{-(f_U+f_L)^3 + 3f_U^3 + 3f_L^3}{27B^2(D-E)} + \frac{D}{3(D-E)} - \frac{E}{D-E} - \frac{2DE^2}{3B^2(D-E)} + \frac{2D^3}{27B^2(D-E)}. \tag{8}$$

Using Eqs. (7) and (8), we can determine the magnitude of the external magnetic field B and the angle θ with the NV axis.

Building on a comprehensive analysis of the experimental principles, we now detail the architecture of our experimental system. Our measurement system consists of an integrated fiber-optic diamond probe, integrated optical path, microwave source, pulse signal generator and signal processing module. The pulse signal generator produces pulses that modulate both the laser and microwave sources. Specifically, the laser emits green light at a wavelength of 532 nm to excite the NV center.[18] The resulting fluorescence signal from the diamond is captured by a photodetector through a long-pass filter. The voltage signal from the avalanche photodiode is then amplified, filtered and processed by the signal processing module.

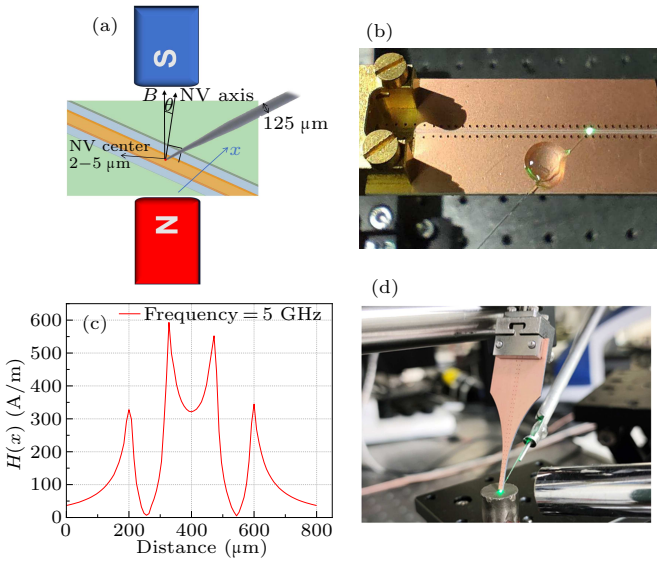


Fig. 1. (a) Schematic diagram of the integrated probe. (b) Physical picture of the integrated probe. (c) Variation of magnetic field component $H(x)$ in the direction of the vertical signal line. (d) Microscopic characterization of a samarium–cobalt permanent magnet.

Figure 1(a) illustrates the fiber-diamond integrated probe, with a micrometer-sized diamond particle affixed to the tip of a conical optical fiber and bonded to a coplanar waveguide signal line. The physical setup is shown in Fig. 1(b). This micrometer-sized sensing area enables the probe to adapt to high-gradient magnetic fields. The coplanar waveguide generates a microwave magnetic field to achieve resonance with the energy levels of the NV center. As shown in Fig. 1(c), variations in $H(x)$ perpendicular to the signal line above the coplanar waveguide help to precisely locate the position of the diamond probe. We position the NV center to the signal line center where the microwave magnetic field is uniform and strong. The coplanar waveguide operates across a broad frequency band, and our analysis at 5 GHz is representative across other frequency ranges. The NV center is processed

with crystal axis orientation,[19] aligning one set of NV axes perpendicular to the coplanar waveguide plane. By placing the fiber-diamond probe in the magnetic field to be measured, we can accurately determine the magnitude and direction of the magnetic field. Figure 1(d) demonstrates the application of the micrometer-resolution magnetic field probe. We have designed a novel coplanar waveguide shape, allowing the diamond NV center to closely approach the surface of the object under test, enabling microscopic magnetic field characterization; this will be discussed in detail later.

3. Uncertainty analysis of magnetic field measurement

Before measuring the magnetic field, we first need to obtain the D and E values of the NV center in the environment. We place the probe inside a magnetic shielding cylinder to shield against interference from the Earth's magnetic field and environmental magnetic fields and then measure a set of zero-field ODMR. In this paper, we use Lorentzian fitting to fit the two peaks; by calculating the difference in the frequencies of the double peaks we obtain the E value and halve the sum of the frequencies to get the D value. Figure 2(a) shows the result of Lorentzian fitting for the two peaks of zero-field ODMR. We can determine that the D value is 2868.85 MHz and the E value is 9.78 MHz. Since we are determining the peak frequency by Lorentz fitting, the uncertainty of the fit is critical. We analyzed the uncertainty of the fit, and performed 20 repeated ODMR measurements under the same experimental conditions. The results were individually Lorentz fitted. The relative deviation of the peak frequency is shown in Fig. 2(b), and the relative uncertainty is better than 5×10^{-5}.

Under a strong magnetic field, the electronic spin energy levels of the NV center split along the direction of the field, resulting in two high-frequency resonance peaks in the ODMR spectrum. As shown in Fig. 2(c), there are three sets of ODMRs at magnetic fields of approximately 10 mT, 300 mT and 1.5 T. By Lorentz fitting, the peak frequencies of the bottom set of ODMRs are 39144.67 MHz and 44873.59 MHz, respectively. Based on the above data, we calculated that the magnitude of the magnetic field is 1498.987 mT, and the angle between the magnetic field and the NV axis is 1.83°.

According to the Hamiltonian, magnetic field measurements depend on the measurement of the D value and the E value, and temperature changes will lead to variations in both D and E values. Although we measure the D and E values for each system after the equipment has stabilized, due to the potential instability of the laser and possible variations in the temperature of the measurement environment we have analyzed the effect of the measurement of the D and E values on the magnetic field measurement. The temperature dependence of the D value is given by $\mathrm{d}D/\mathrm{d}T = -74.2(7)$ kHz·K^{-1}.[10] Assuming an environment at room temperature, where $D = 2.87$ GHz, the uncertainty in measuring the magnetic field with D value changes of 0.1 MHz, 0.5 MHz and 1 MHz is shown in Fig. 2(d). It can be seen that in a strong magnetic environment the impact of temperature changes on magnetic field measurements is very small and the error can be considered negligible. However, when the magnetic field is low, temperature changes have a larger impact on magnetic field measurements and the effect of D and E on field measurement should be corrected. This can be done by integrating a temperature sensor on the probe to measure the temperature in real time and compensate for the D value, thus eliminating the effect of temperature changes on magnetic field measurements. At the same time we also conduct an error analysis of the impact of E value measurements on magnetic field measurements, as shown in Fig. 2(e), where the relationship between E value and temperature is $\mathrm{d}E/(E\,\mathrm{d}T) = -1.4(3) \times 10^{-4}$ K^{-1}.[20] The E value is minimally affected by temperature and has a small impact on magnetic field measurements.

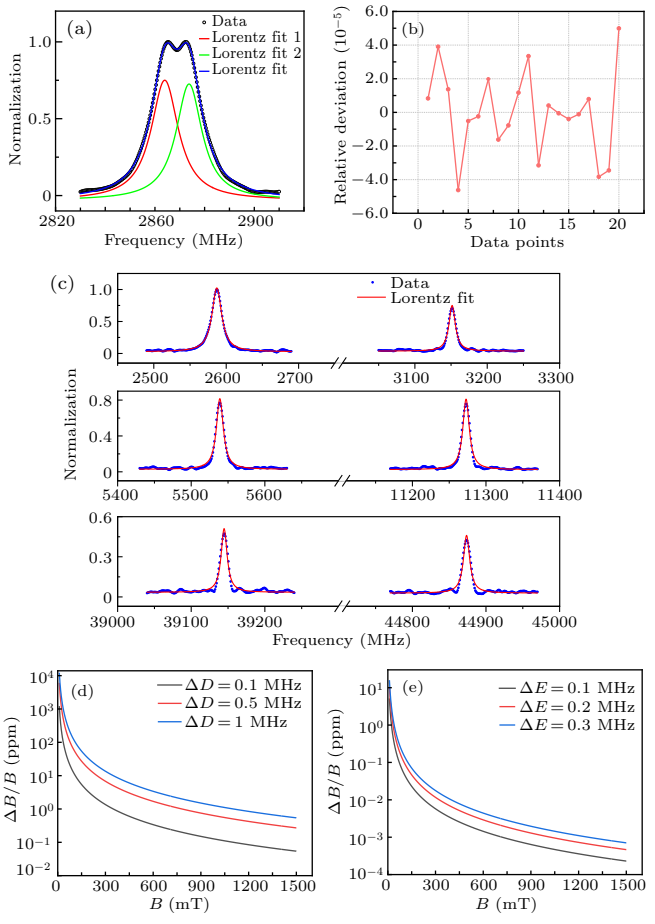


Fig. 2. (a) Fitting results of zero-field ODMR by Lorentz fitting. (b) The uncertainty of resonance frequency by Lorentzian fitting. (c) The ODMR spectrum and its fitting results under magnetic fields of 10 mT, 300 mT and 1500 mT. Uncertainty analysis of the effect of D (d) and E (e) on magnetic field measurements.

4. Experimental verification

We conducted testing and verification of the diamond magnetometer within the range of 10 mT to 1.5 T using a 0.1–50 mT constant magnetic field standard device and a 50 mT to 2.0 T constant magnetic field standard device, both with a relative uncertainty better than 2×10^{-5} and annual stability of better than 3.5×10^{-5}. In the range of 10–50 mT, the amplitude of the standard magnetic field was obtained through the relationship between current and magnetic field (5.2426 mT·A^{-1}), and from 50 mT to 1.5 T, the measurement value of the NMR probe PT2026 was used as the standard magnetic field strength. We selected 20 magnetic field values for testing, using the standard magnetic field size and the diamond magnetometer measurement values as the horizontal and vertical axes of the Cartesian coordinate system, respectively. The result of fitting a straight line was $y = 1.00011x - 0.11985$, as shown in Fig. 3(a). Thus, a measurement nonlinearity error of 0.0028% can be obtained from the fitting equation and the original data. The formula for calculating the nonlinearity error is

$$\delta = \frac{\Delta Y_{\max}}{Y} \times 100\%, \tag{9}$$

where $\Delta Y_{\max}$ is the maximum deviation between the sensor calibration curve and the fitted straight line and Y is the full-scale output. Additionally, we conducted 15-min stability tests at magnetic fields of 45 mT, 300 mT and 1.5 T, collecting 100 magnetic field values each time, as shown in Fig. 3(b). The results indicate that the stability is better than 0.015% at a 45 mT magnetic field, better than 0.004% at a 300 mT magnetic field and better than 0.0012% at a 1.5 T magnetic field.

By conducting micro-characterization of permanent magnets, we can gain profound insights into their microstructure. Such an approach is instrumental in enhancing the properties of current materials and lays a crucial foundation for the innovation of advanced, high-performance permanent magnet materials. Leveraging the micrometer resolution capability of the diamond NV center, we characterized the magnetic field on the surface of samarium–cobalt permanent magnets, with the test environment shown in Fig. 1(d). The object under test was a cylindrical samarium–cobalt permanent magnet with a height and diameter of 1 cm. We designed a new shape for the coplanar waveguide, allowing the diamond NV center to closely approach the surface of the magnet. The diamond NV center underwent crystal axis orientation treatment, with one set of NV axes perpendicular to the surface of the magnet.

A 750 μm^2 area near the center of the magnet's surface was selected as the scanning area, with a scanning step of 5 μm. We performed microscopic characterization of the magnitude and angle of the magnetic field at heights of 80 μm and 330 μm from the surface of the magnet.

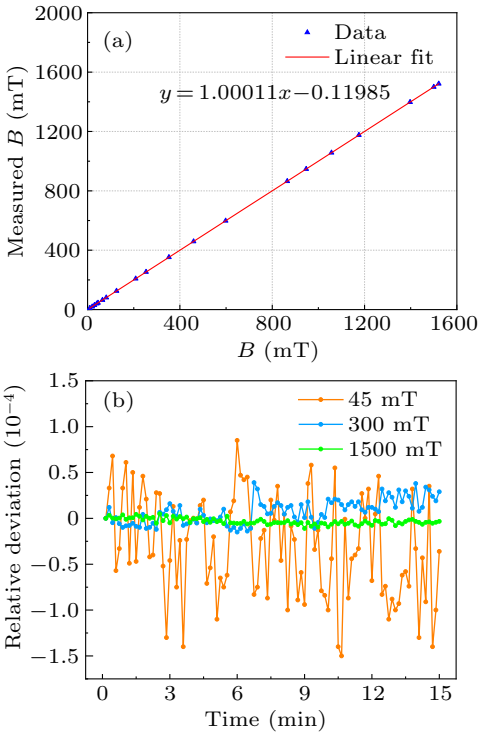


Fig. 3. (a) The linear fitting result for the measured magnetic field to the standard magnetic field. (b) Stability testing under different magnetic fields.

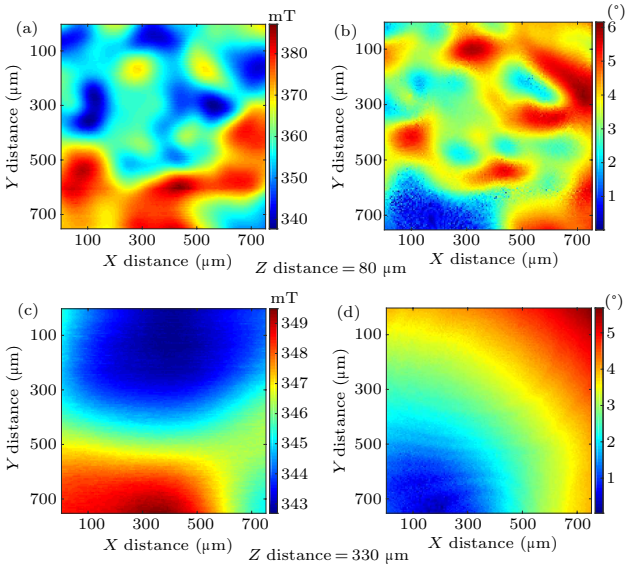


Fig. 4. (a) Magnetic field imaging at a distance of 80 μm from the surface of a samarium–cobalt permanent magnet. (b) Magnetic field angular imaging at a distance of 80 μm from the surface of a samarium–cobalt permanent magnet. (c) Magnetic field imaging at a distance of 330 μm from the surface of a samarium–cobalt permanent magnet. (d) Magnetic field angular imaging at a distance of 330 μm from the surface of a samarium–cobalt permanent magnet.

Figures 4(a) and 4(c) show the distribution of the magnetic field magnitude at heights of 80 μm and 330 μm from the surface of the magnet, respectively. Figures 4(b) and 4(d) show the distribution of the angle between the magnetic field and the NV axis at the same heights. As can be seen from the figures, the closer the imaging is to the surface of the magnet, the more the microstructural features of the crystal grains lead to microscopic variations in the magnetic field. This proves that

our probe has a micrometer-level resolution and holds significant promise in the field of microscopic characterization of magnetic materials.

5. Conclusion and perspectives

In conclusion, we have designed a quantum precision magnetometer with a range of 10 mT to 1.5 T by immobilizing diamond NV centers on the surface of a coplanar waveguide. We have analyzed the sources of error in the magnetometer and proposed solutions accordingly. Subsequently, we tested its performance and found that its measurement nonlinearity error is better than 0.0028%, while its stability under a 1.5 T magnetic field exceeds 0.0012%. Finally, we demonstrated its application in micro-characterization on the surface of permanent magnets, achieving excellent microscopic imaging results due to its superior resolution of better than 3 μm. This observation is a testament to the micrometer-level resolution capability of our probe, underscoring its significant potential for applications in the microscopic characterization of magnetic materials — a field ripe for discovery and innovation.

Acknowledgements

Project supported by the National Key R&D Program of China (Grant No. 2021YFB2012600). We acknowledge calibration support by Tieying Feng of Jiangsu Institute of Metrology.

References

[1] Khan M A, Sun J, Li B D, Przybysz A and Kosel J 2012 *Eng. Res. Express* **3** 022005
[2] Javor J, Stange A, Pollock C, Fuhr N and Bishop D J 2020 *Microsyst. Nanoeng.* **6** 71
[3] Li Z, Ouyang Z R, Leng Z K, Zhang Y B, Zhang S, Lu Y F and Yan Z D 2022 *Electronics* **11** 970
[4] Wang X L and Wang F H 2020 *J. Magn. Mater. Devices* **6** 63
[5] Xu Z, Liu J and Zhang X X 2013 *Modern Electronics Technique* **12** 29
[6] Qu S S and He Z W 2013 *Electrical Measurement & Instrumentation* **50** 98
[7] Li X, Xiao L Z, Liu H B, Zhang Z F, Guo B X, Yu H J and Zong F R 2013 *Acta Phys. Sin.* **62** 147602 (in Chinese)
[8] Jelezko F, Gaebel T, Popa I, Gruber A and Wrachtrup J 2004 *Phys. Rev. Lett.* **92** 076401
[9] Maze J R, Stanwix P L, Hodges J S, Hong S, Taylor J M, Cappellaro P, Jiang L, Gurudev Dutt M V, Togan E, Zibrov A S, Yacoby A, Walsworth R L and Lukin M D 2008 *Nature* **455** 644
[10] Li Z H, Wang T Y, Guo Q, Guo H, Wen H F, Tang J and Liu J 2021 *Acta Phys. Sin* **70** 147601 (in Chinese)
[11] Dong M M, Hu Z Z, Liu Y, Yang B, Wang Y J and Du G X 2018 *Appl. Phys. Lett.* **113** 131105
[12] Pham L M, Sage D L, Stanwix P L, Yeung T K, Glenn D, Trifonov A, Cappellaro P, Hemmer P R, Lukin M D, Park H, Yacoby A and Walsworth R L 2011 *New J. Phys.* **13** 045021
[13] Duan D, Du G X, Kavatamane V K, Arumugam S, Tzeng Y K, Chang H C and Balasubramanian G 2019 *Opt. Express* **27** 6734
[14] Yahata K, Matsuzaki Y, Saito S, Watanabe H and Ishi-Hayase S 2019 *Appl. Phys. Lett.* **114** 022404
[15] Gruber A, Dräbenstedt A, Tietz C, Fleury L, Wrachtrup J and von Borczyskowski C 1997 *Science* **276** 2012
[16] Doherty M W, Michl J, Dolde F, Jakobi I, Neumann P, Manson N B and Wrachtrup J 2014 *New J. Phys.* **16** 063067
[17] Barson M S J, Krausz E, Manson N B and Doherty M W 2019 *Nanophotonics* **8** 1985
[18] Manson N B, Harrison J P and Sellars M J 2006 *Phys. Rev. B* **74** 104303
[19] Chen G B, Gu B X, He W H, Guo Z G and Du G X 2020 *IEEE J. Quantum Electron.* **56** 7500106
[20] Acosta V M, Bauch E, Ledbetter M P, Waxman A, Bouchard L S and Budker D 2010 *Phys. Rev. Lett.* **104** 070801